Dalton Transactions

ROYAL SOCIETY OF CHEMISTRY

PAPER

View Article Online
View Journal | View Issue

Check for updates

Cite this: *Dalton Trans.*, 2026, **55**, 2948

Combustion synthesis of $(U,Pu)O_2$ solid solution: from parametric study to sintered pellet

Anna Hautecouverture, [a,b] Paul Estevenon, *[b] Elena Bazarkina, [c,d] Kristina Kvashnina, [c,d] Philippe Martin, [b] Florent Lebreton, [b] Cyrielle Rey [a] and Xavier Deschanels [a]

Received 6th September 2025,
Accepted 26th December 2025

DOI: 10.1039/d5dt02138c

rsc.li/dalton

This study presents the synthesis of actinide mixed oxides by solution combustion synthesis (SCS) using citric acid as fuel. The approach was chosen because of the promising results on surrogates and both uranium and plutonium pure oxides. The amount of fuel for SCS and the effect of the Pu/(U + Pu) composition were studied to optimize the characteristics of the powders. A solid solution $(U,Pu)O_{2+x}$ was obtained for all conditions, and the resulting oxides exhibit a homogeneous cationic distribution of uranium and plutonium and nanometric features. A $U_{0.90}Pu_{0.10}O_{2+x}$ powder was selected for pressing tests and sintering due to its industrial interest for the production of MOX fuel for PWR reactors. It was possible to obtain a pellet with a density of 88%TD, characterized by a low-temperature sintering due to the nanometric size of the powder. Despite presenting large macropores, due to the presence of residual carbon in the powder before sintering, the sintered pellet presents the expected round-shaped pores and a very homogeneous plutonium distribution.

Introduction

Nuclear power is an important source of low-carbon energy, providing approximately 10% of the world's electricity. In nuclear reactors, uranium fission leads to the formation of fission products and transuranic compounds formed by neutron capture and β-decay.[1] For PWR reactors with UO_2 fuel enriched to 3.5% ^{235}U, irradiated for 3 years at 33 GW day per t, the spent fuel contains approximately 95.5 mass% of uranium, 3.5 mass% fission products, 0.9 mass% plutonium, and approximately 0.1 mass% minor actinides (Np, Am, Cm, *etc.*).[2] Plutonium and minor actinides are the main contributors to the long-term radiotoxicity of spent nuclear fuel.[3] Managing these transuranic elements poses significant challenges concerning the long-term environmental impact, societal issues associated with nuclear waste storage, and storage conditions, as the radioactivity of these elements affects the thermal properties of storage. Spent fuel recycling is a tool to manage nuclear waste by reducing by a factor of 5 the volume of the waste generated by the fuel and by a factor of 10 its activity.[4] In addition, plutonium has fissile isotopes ^{239}Pu and ^{241}Pu, which represent an energy potential. One promising solution to these problems is recycling the valuable elements in the spent fuel through the production of Mixed OXide (MOX) fuel, which is composed of $(U,Pu)O_2$ oxide. The use of MOX fuel can significantly reduce the amount of long-lived nuclear waste generated, as well as decrease the demand for uranium resources,[5] as a closed cycle of MOx production decreases by 25% the need for uranium.[4]

Despite the potential benefits of MOX fuel, its fabrication is a complex and challenging process. In particular, the production of homogeneous MOX fuel has proven to be difficult due to the different physical and chemical properties of the two powders.[6,7] Indeed, the preparation of MOX fuel is generally achieved by a multi-step process, including mixing and grinding of plutonium and uranium dioxide powders before shaping and sintering to obtain pellets.[8–10] Additionally, the production of plutonium dioxide through oxalic precipitation and calcination may result in residual carbon contamination of the powder, which can lead to challenges in the sintering process.[11]

In recent years, significant progress has been made in the development of MOX fuel fabrication techniques, including the development of new powder metallurgy techniques, the use of advanced ceramic materials, and new sintering processes.[12,13]

In addition to the advances in homogeneous MOX fuel fabrication using powder metallurgy, there is also interest in developing a liquid-based synthesis method for MOX

[a]*ICSM, Univ Montpellier, CNRS, CEA, ENSCM, Bagnols-sur-Cèze, France*
[b]*CEA, DES, ISEC, DMRC, Univ Montpellier, Marcoule, France.*
E-mail: paul.estevenon@cea.fr
[c]*The Rossendorf Beamline at ESRF, CS 40220, 38043 Grenoble Cedex 9, France*
[d]*Helmholtz Zentrum Dresden Rossendorf (HZDR), Institute of Resource Ecology, 01314 Dresden, Germany*

fuel.[12,14–23] This approach involves dissolving plutonium and uranium in a suitable solvent, followed by precipitation and sintering to produce the final fuel. The liquid-based synthesis methods offer greater homogeneity of the nuclear fuel without requiring a grinding step, limiting the dispersion of fine particles. This could enable the production of MOX fuels with optimized isotopic compositions, leading to improved fuel burnup and reduced waste generation.

Among the liquid routes, another promising approach to the fabrication of MOX fuel is through the combustion of actinide oxides in solution.[24–26] Compared to sol-gel or precipitation synthesis methods, these synthesis methods offer the advantage of being very simple to implement, greatly minimizing effluent production and potential actinide leaks, and relying on a very fast reaction, making them highly capacitive. Solution combustion synthesis (SCS) was discovered in the 1970s.[24] It is a self-propagating, exothermic process used to prepare materials, including oxide powders, for various applications such as energy fuels, catalysts, and electrodes.[27,28] The SCS involves a redox reaction between a metal nitrate (oxidant) and an organic compound (reducing agent) dissolved in aqueous solution. The first step in SCS is the dehydration of the solution to form a dried solid gel containing the reactants. Further thermal treatment results in ignition within the mixture, which is characterized by its rapidity and strong exothermicity. It allows high temperatures (500 °C–1500 °C)[27,29] to be reached in a short time range with low energy input, as the ignition temperature is typically low (200 °C–250 °C).[30–32] The size of the resulting mixed oxide particles is determined by the ignition process.[27,33]

The SCS method can lead to the formation of mixed oxides with homogeneous cation distribution, and the resulting powder characteristics are strongly correlated to the flame temperature reached during combustion.[29,34,35] The selection of the fuel for the combustion is critical, and the stoichiometric amount of fuel required for the reaction can be determined based on the reactants and the fuel-over-metal molar ratio (Fuel/Metal).[36] According to the theory developed by Jain *et al.*, it is possible to calculate the stoichiometric conditions of the reaction by considering the reducing and oxidizing valences of the species (V_{Fuel} and V_{Metal}).[36] Under equilibrium, the reaction is stoichiometric when the richness parameter ϕ defined by Jain is equal to one, according to:

$$\phi = \frac{V_{Fuel}}{V_{Metal}} \times \frac{n_{Fuel}}{n_{Metal}} = 1$$

where n_{Fuel} and n_{Metal} are the stoichiometric coefficients of the SCS reaction (see the SI).

The synthesis of actinide oxide (UO_2 and PuO_2) by SCS, with citric acid (CA) as fuel for the combustion, has been reported.[30,32,37] Studies have shown that it is possible to reduce U(+VI) into U(+IV) to obtain UO_{2+x} with the SCS method without further reducing treatment. The oxides obtained by this method exhibit small crystallite sizes. The optimal fuel/metal ratio was experimentally determined for the plutonium/citric acid and uranium/citric acid systems[37,38] to be 0.6 and 1.1, respectively, considering the characterizations of the powders after the combustion.

The SCS method also proved to be of interest for mixed oxides. Indeed, several studies reported the synthesis of (U,Ce)O_2 oxides with the SCS method using citric acid and glycine,[32,33,39–41] but only a few studies have examined the effect of the fuel/(U + Ce) ratio on the powders. Maji *et al.*[33] and Monnier[32] reported the synthesis of $U_{0.5}Ce_{0.5}O_2$ using citric acid and glycine, with the fuel/metal ratio varying.

The aim of this work is to present the results of the first synthesis of (U,Pu)O_2 oxides by SCS with citric acid. The effect of the fuel/metal ratio was studied on $U_{0.5}Pu_{0.5}O_2$ synthesis in order to determine the optimal conditions for the combustion. Furthermore, using these results, the MOX synthesis was tested for different Pu contents to assess the efficiency of the synthesis method in order to produce fuels with different levels of Pu doping.

Experimental

Chemicals

Caution: ^{238}Pu, ^{239}Pu, ^{240}Pu and ^{242}Pu are α-emitters, and ^{241}Pu is a β^--emitter, which are considered as health risks. Experiments involving actinides require appropriate facilities for handling radioactive materials. Experiments were conducted at the ATALANTE facility (Marcoule Center, France) in a glovebox under air or nitrogen (pellet fabrication and characterization) atmosphere. The criticality risk associated with the use of plutonium was controlled in our case by the mass of plutonium considered. In the case of scaling up, the subcritical geometry of industrial equipment should be considered.

The plutonium solution (isotopic composition of ^{238}Pu (0.1%), ^{239}Pu (84.9%), ^{240}Pu (14.3%), ^{241}Pu (0.3%) and ^{242}Pu (0.4%)) was purified *via* a standard anion–exchange method in order to remove ^{241}Am, which is produced by the β decay of ^{241}Pu. Plutonium was stabilized in the +IV oxidation state in 1.9 mol L^{-1} HNO_3 solution in order to avoid hydrolysis. Plutonium stock solution was titrated using a UV-visible spectrophotometric method, on a Varian Cary 6000i device using diluted mother solution in 1.0 mol L^{-1} HNO_3 media. The signal was deconvoluted from certified Pu(+III), Pu(+IV) and Pu(+VI) reference samples, in 1.0 mol L^{-1} HNO_3 media, to obtain a value of C_{Pu} = 0.22 ± 0.02 mol L^{-1}.

Uranyl nitrate was obtained by dissolution of U_3O_8 powder in nitric acid. The solution was then dehydrated at 180 °C in order to obtain a yellow powder, which was ground in an agate mortar and characterized.

Citric acid $C_6H_8O_7$ (Sigma Aldrich ACS reagent grade, purity ≥99.5%) was used as fuel for the SCS reaction.

Synthesis

200 mg of actinides were used for each combustion with several compositions (*i.e.* Pu/(U + Pu) ratio). Solutions for combustion synthesis were prepared by dissolving the appropriate amount of citric acid and uranyl nitrate in plutonium nitric

solution. The solution was diluted with 1 mol L^{-1} HNO_3 in order to keep $C_{NO_3^-}$ = 1.9 mol L^{-1}, as in previous work.[37]

First, the effect of the amount of citric acid (CA/(U + Pu) ratio) was studied in the range 0.6 to 1.2 to determine the optimal ratio with a set composition containing 50 mol% uranium and 50 mol% plutonium. Once the optimal ratio was determined, the effect of the composition was studied by producing samples from 11 mol% Pu to 50 mol% Pu.

After dissolution of the fuel in the actinide nitric solution, the solutions were dehydrated in an alumina crucible on a hot plate at 120 °C for one hour to obtain a dried gel containing the reactants. The resulting gel was then heated in a Lenton tubular furnace, under a 10 NL h^{-1} air flow, from 120 °C to 300 °C at 10 °C min^{-1} heating rate, to ensure gel dehydration, with a final 10 min step at 300 °C, allowing the sample to reach this setpoint temperature. After cooling to room temperature, the obtained powder was ground in an agate mortar. The powders were characterized as-prepared before a further thermal treatment under reducing atmosphere (Ar-96%/H_2-4%) for 1 h at 1100 °C.

Characterization

X-ray diffraction characterization of the powders was performed with a Bruker D8 diffractometer equipped with a Lynxeye detector and using Cu Kα radiation (λ = 1.54184 Å) and Bragg-Brentano geometry. The powders were prepared in adapted sample holders in order to avoid any potential radioactive contamination. XRD patterns were recorded at room temperature in the $10° \leq 2\theta \leq 100°$ range with a step size of 0.02° and a counting time of 2 s per step. Metallic gold (99.96%, Alpha Aesar) was used as an internal standard in order to calibrate the angular positions of the observed XRD, in accordance with PDF 00-004-0784.[42] The addition of this internal standard is necessary due to the method of preparing radioactive samples for XRD analysis, which can have a significant impact on specimen height. Metallic gold was chosen as a standard because of its chemical stability, which avoids lattice parameter variation, and because the peaks of the fluorite phase of gold do not overlap with those of $(U,Pu)O_{2\pm x}$. FullProf software was used for XRD data treatment.[43] The refinements were carried out by approximating the peaks obtained on the experimental XRD-patterns with the modified Thomson Cox-Hastings pseudo-Voigt profile function (TCH-Z). Lattice parameters were calculated using the Rietveld method. The crystallite sizes were determined by refining the parameters of the Lorentzian component after subtracting the experimental contribution of the diffractometer to the peak broadening. For this, a reference sample of LaB_6 was measured and its Gaussian contributions were retained for subtraction.

Thermogravimetric analysis (TG) of the resulting powders was carried out in flowing air up to 1100 °C at a heating rate of 5 °C min^{-1} using a STA449 Netzsch device coupled with micro-gas chromatography modules (μGC). The residual carbon content of the powders was calculated by integrating the signal of CO and CO_2 peaks obtained in μGC, using two Agilent 3000 modules (non-polar gas module with a molecular sieve as the stationary phase and polar gas module with grafted silica as the stationary phase) with a micro thermal conductivity detector (TCD) and He used as vector gas. μGC calibration was achieved by using gas bottles containing calibrated CO and CO_2 concentrations ranging from 500 to 10 000 ppm (Air Liquide).

Scanning Electron Microscopy (SEM) observations were conducted using powder samples deposited on carbon adhesive sticks and metallized with gold, using a Tescan Mira3 electronic microscope equipped with a secondary electron detector (SE) under high-vacuum conditions with an accelerating voltage of 5 kV.

The HERFD-XANES experiments were performed at beamline BM20 of the European Synchrotron Radiation Facility (ESRF) in Grenoble (France).[44] The incident energy was selected using the [111] reflection from a double-crystal Si monochromator. Two mirrors, placed before and after the monochromator, were used to collimate the beam and suppress higher harmonics. The beam size was estimated to be ~50 μm (vertically) by ~2 mm (horizontally). HERFD-XANES spectra at the M_4 edge (3728.0 eV for U and 3970.0 eV for Pu) were recorded with an X-ray emission spectrometer,[45] by measuring the intensity of the U M_β (3339.8 eV) or Pu M_β (3534.0 eV) emission line as a function of the incident energy near the corresponding M_4 edge. The spectrometer was aligned separately for each actinide using oxides UO_2 or PuO_2. The alignment was performed in the non-resonant emission mode (*i.e.* with incident energy above the X-ray absorption edge) by selecting the maximum of the corresponding emission line. The emission energy was selected using the [220] reflection of five spherically bent Si crystal analyzers (1 m bending radius) aligned at specific Bragg angles: 75.2° for U and 66.0° for Pu. The optical paths of the emitted X-rays were optimized using a helium-gas-filled bag to minimize intensity losses due to air absorption. The calibration of the incident energy was performed by assigning the maximum of the HERFD-XANES spectrum of UO_2 to 3725 eV, and that of PuO_2 to 3971 eV. The measurements were conducted at 25 °C. 1 mg of powder was diluted with 200 mg of boron nitride and pressed into a pellet. The pellet was sealed in a specific sample holder consisting of two nested screwed envelopes and a Kapton window (5 μm). This multi-confinement method was chosen in order to allow the manipulation of the radioactive sample under safe conditions, with non-contamination controls performed on both sample envelopes. The measured HERFD-XANES spectra were deconvoluted with a reference dataset using the Microsoft Excel solver. A linear combination of references was used to generate a model. Each reference corresponds to a specific oxidation state of actinide (see the SI for descriptions of the references).

The particle size distribution of the powder was measured using a Malvern Spraytec device. A fraction of the powder was diluted in 100 mL of water with a drop of dispersant (Dolapix CE 64). The solution was maintained under constant stirring to avoid particle precipitation and to ensure circulation of the

solution in the measurement cell. The curves resulting from the merging of three data sets were recorded.

Pellet shaping and sintering

700 mg of the $U_{0.90}Pu_{0.10}O_{2+x}$ powder was used for pellet shaping using an Osterwalder automatic hydraulic floating press at 450 MPa in a 6.08 mm die. The densification behavior of the pellet was studied using a DIL402 E/7 Netzsch horizontal dilatometer. The furnace was composed of a graphite heating resistor protected by an alumina tube. The temperature heat treatment was composed of three phases: a heat ramp to 1700 °C at 2 °C min^{-1}, an isothermal heating at 1700 °C for 4 hours, and a temperature decrease to room temperature at 6 °C min^{-1}. The treatment atmosphere was set to Ar 95.7%/H_2 4.3% with 1200 vpm of H_2O (corresponding to pO_2 = 4.3 × 10^{-26} atm at 650 °C) using a Setnag GenAir zirconia-based oxygen pump gauge.

The sample density was determined by hydrostatic measurement based on the weight of the dry sample, immersed in bromobenzene, and finally impregnated with bromobenzene at a controlled temperature. These measurements were replicated three times, enabling the determination of the sample's hydrostatic density compared to the theoretical density of the oxide (%TD), as well as the open and closed porosity of the pellet.

The $U_{0.90}Pu_{0.10}O_{2+x}$ pellet was mounted in a polyester resin and submitted to a longitudinal cut and a mirror polish. Optical imaging was performed with an optical microscope installed by Optic Peter and equipped with objectives and a camera (Olympus). The porosity size analysis (which also provides an estimation of the total porosity) was performed by means of the FIJI software.[46]

The uranium-plutonium spatial distribution in the polished pellet was characterized using a CAMECA SX100 electron probe microanalyzer, in which the electron source is made of a tungsten wire. Before analysis, the sample was coated with a few tens of micrometers of carbon. Measurements were performed at 20 kV, with a probe current of 50 nA. The data were collected at the O K_α (524.9 eV), U Mα (3170.8 eV) and Pu M_β (3534 eV) fluorescence lines. The Pu M_β line was used instead of PuM_α (3345 eV) in order to avoid interference with the U M_β line (3336.7 eV). Under these conditions, the probed volume for the actinides M lines in $(U,Pu)O_2$ is about 0.8 μm in diameter and 0.5 μm in depth (as calculated with the CASINO V3.3 Monte Carlo software[47]). 2D maps were collected by stage mapping, each for an area of 1024 × 1024 μm^2, with vertical and horizontal steps of 1 μm, a counting time of 20 ms per step on the peak, without background subtraction. For a better description of the plutonium distribution homogeneity, an additional mapping was recorded at 200 nA with a counting time of 100 ms per step, over a 512 × 512 μm^2 area. Quantitative measurements were performed along several 800 μm long lines with a 1 μm step and counting times of 15 s on the peak and 2 × 5 s on the background. Mass fractions were obtained using the X-PHI method[40] integrated in the CAMECA Peak Sight V6.5 software, using a UO_2 pellet for O and U calibrations and a PuO_2 pellet for Pu. The interference of the U M_γ (3521.0 eV) signal on the Pu M_β was corrected, using the same UO_2 pellet. The Pu maps were then pseudo-quantified using a linear relation between the count number and the Pu content.[2] The parameters were determined by comparing the count number in the Pu maps distribution to that of the Pu mass fraction measured along the lines.

The oxygen stoichiometry (O/M ratio with M = U + Pu) in the polished pellet was evaluated using Raman spectroscopy. Data were acquired using a Horiba Jobin-Yvon iHR320 Raman spectrometer coupled *via* optical fibers to a confocal optical microscope. The measurements were performed with a ×100 objective lens and a green laser (λ = 532 nm), along a 1200 groove per mm grating. This configuration enables a resolution of ±1 cm^{-1}.[48] The incident power was limited to 1.0 mW in order to preserve the integrity of the surface. The reproducibility of the spectra was verified by repeated acquisitions on the same areas, which revealed no modification of the Raman signal. To ensure frequency accuracy, a silicon standard with a Raman line frequency of 520.5 cm^{-1} was used to calibrate the spectrometer. Subsequently, light from a neon lamp was introduced into the path of the scattered light to ensure a permanent frequency calibration of the spectrometer. The resulting instrumental uncertainty on the position of the Raman lines was estimated at ±0.5 cm^{-1}. The spectra were collected between 90 and 1960 cm^{-1}. To assess its homogeneity, spectra were collected along a 3 mm line (whole diameter of the pellet) with a 2 μm step. In total, 1851 spectra were acquired with an acquisition time of 60 s per point, and two successive acquisitions to improve the signal-to-noise ratio. The data acquisition and treatment were performed using the LabSpec v6.7.1.10 software (Horiba). The background was modelled using a linear function. Thereafter, each Raman band was fitted with a combination of mixed functions (Gaussian + Lorentzian) of the same frequencies and widths, enabling the determination of the position, width, and intensity of each band.

Results and discussion

Effect of fuel/metal ratio on $U_{0.5}Pu_{0.5}O_{2\pm x}$ oxides synthesis

The influence of the CA/(U + Pu) ratio on the reduction of uranium(+VI) to uranium(+IV) has been previously demonstrated in the literature. In these studies, a secondary U_3O_8 phase can be observed in some cases, depending on the ratio considered, indicating the presence of residual uranium(VI) that was not reduced during combustion.[32,38,41,49] However, the reducing conditions can be reached under a specific CA/(U + Pu) ratio, as previously reported in the literature.[30,32,41] Such a situation can also be observed in the synthesis of mixed uranium and cerium oxides, where the $(U,Ce)O_2$ fluorite phase can be observed along with a secondary uranium-rich U_3O_8 phase.[32,33,37,41]

In the present case, diffraction patterns of the powders containing 50 mol% uranium and 50 mol% plutonium show the

formation of a single-phase compound, with no evidence of a secondary phase (Fig. 1). The obtained oxides all crystallized in a fluorite-type structure, $U_{0.5}Pu_{0.5}O_{2\pm x}$.

However, the lattice parameter of the $U_{0.5}Pu_{0.5}O_{2\pm x}$ oxides is significantly lower than the theoretical lattice parameter according to Vegard's law between the pure UO_2 and PuO_2 endmembers (a = 5.4335 Å)[50–52] (Table 1), which could indicate an over-stoichiometry of the oxides. This difference seems to be particularly sensitive in the case of the oxide obtained with a low CA/(U + Pu) mole ratio, which may indicate an insufficient amount of citric acid for the reduction of uranium, or that the SCS reaction does not lead to complete uranium reduction under these combustion conditions.

The effect of the fuel/metal ratio on the crystallinity of oxides obtained by SCS has been demonstrated for plutonium oxides,[37,38] or cerium oxides.[34] In the literature, the increase in the size of cerium oxide CeO_2 crystallites has been attributed to an increase in flame temperature.[34] Optimal ratios for the combustion of plutonium nitrate and uranyl nitrate into PuO_2 and UO_2 with citric acid have been determined to be 1.1[37] and 0.6,[38] respectively.

The crystallite sizes calculated from the X-ray patterns range between 9 (±1) and 30 (±1) nm and reach a maximum value for the CA/(U + Pu) ratio between 0.73 and 0.89 (Table 1). These results are consistent with the crystallite size previously determined for pure PuO_2 and UO_2 samples obtained by SCS reaction with the optimal ratio (26 ± 1 nm and 51 ± 1 nm, respectively).[37,38] The crystallite sizes are small due to the almost instantaneous ignition and rapid dissipation of heat during the SCS reaction.

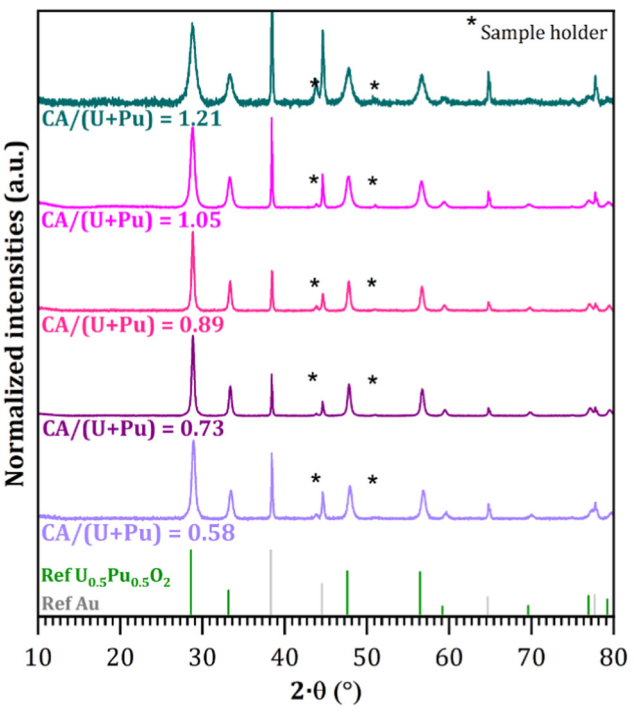

Fig. 1 X-ray patterns of $U_{0.5}Pu_{0.5}O_{2\pm x}$ powders obtained by citric acid assisted SCS in an air atmosphere.

Table 1 Crystallographic data and residual carbon content of $U_{0.5}Pu_{0.5}O_{2\pm x}$ powders obtained by citric acid assisted SCS (theoretical value of lattice parameter for $U_{0.5}Pu_{0.5}O_{2\pm x}$: a = 5.4335 Å)

CA/(U + Pu) ratio	Lattice parameter, a (Å)	Crystallites size (nm)	Residual carbon content (%mass.)
1.21	5.408(2)	8 ± 1	2.4 ± 0.2
1.05	5.4094(1)	15 ± 1	1.5 ± 0.1
0.89	5.4073(1)	27 ± 1	0.3 ± 0.1
0.73	5.4061(1)	30 ± 1	0.8 ± 0.1
0.58	5.3921(1)	16 ± 1	1.2 ± 0.1

Therefore, based on the PXRD results, the optimal CA/(U + Pu) molar ratio to trigger the SCS reaction seems to be between 0.73 and 0.89. This reaction led to oxide phases with a characteristic fluorite structure that exhibit lattice parameters significantly lower than the values expected for $U_{0.5}Pu_{0.5}O_2$, which could be correlated to an over-stoichiometry of the oxides (Table 1).

The hypothesis of an over-stoichiometry of the oxides has been studied with the aid of HERFD-XANES measurements performed at the uranium and plutonium M_4 edges on the powder with an initial ratio CA/(U + Pu)/An = 0.89. The spectra obtained clearly indicate the presence of a very large amount of uranium(+V) and (+VI) in the sample (Table 2), corresponding to approximately 44% and 55% of the uranium content, respectively. This very high level of overoxidation, which exceeds that generally accepted for actinide oxides with a cubic structure, can be explained both by the stabilization of the cubic phase by the presence of the plutonium, and by the kinetics of the SCS reaction (very rapid temperature rise during combustion followed by thermal quenching), which do not favor the exsolution of uranium oxide. The HERFD-XANES measurement performed at the plutonium M_4 edge evidence that plutonium is mainly in the +IV oxidation state in the oxide (contribution around 85%), but that there is also a significant contribution of plutonium in the +V oxidation state (contribution around 13%), which is rarely encountered in the oxides,[53] as will be discussed further in the article. These results lead to an estimate of the empirical formula of the over-stoichiometric oxide as being $U_{0.5}Pu_{0.5}O_{2.4}$.

The SCS method, which involves the use of organic molecules, can result in residual carbon contamination in the obtained powders. A high CA/(U + Pu) ratio can lead to a significant amount of residual organic content (Table 1) while a low CA/An ratio leads to a lack of organic reactant and therefore an incomplete combustion.[28,54] Thus, the smallest carbon contamination should be obtained for the stoichiometric reaction. Optimal ratios for the combustion of plutonium nitrate and uranyl nitrate into PuO_2 and UO_2 with citric acid have been determined as 1.1[37] and 0.6,[38] respectively, considering a maximum crystallite size and a minimum carbon content. In this study, the smallest carbon contents were found for samples with a CA/(U + Pu) ratio between 0.73 and 0.89, in line

Table 2 HERFD-XANES spectra recorded at the uranium (left) and plutonium (right) M_4 edges for the powders $U_{0.5}Pu_{0.5}O_{2+x}$ powder, synthesized with CA/(U + Pu) = 0.89, and deconvolution results

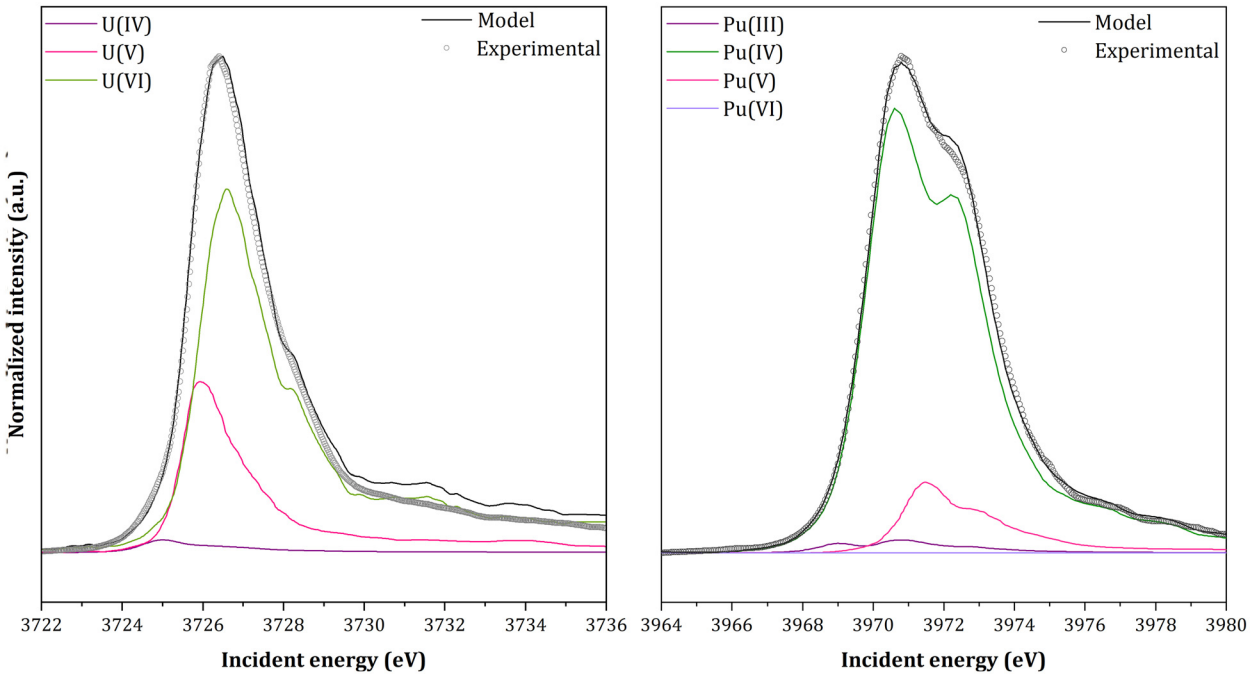

Oxidation state	Contribution in $U_{0.50}Pu_{0.50}O_{2+x}$ powder[a]
Uranium(+IV)	1%
Uranium(+V)	44%
Uranium(+VI)	55%
Plutonium(+III)	2%
Plutonium(+IV)	85%
Plutonium(+V)	13%
Plutonium(+VI)	0%

[a] For the quantification of the different oxidation states, the error is estimated as 5%.

with the value previously determined from crystallite size determination.

Since the optimal CA/(U + Pu) ratio also seems to be located in the range between 0.73 and 0.89 for a 50/50 mixture, based on both the crystallite size and the carbon contamination of the oxide formed, it appears to be coherent with a linear or pseudo-linear relationship between the uranium and plutonium pure poles (experimentally determined to be 1.1 and 0.6, respectively,[37,38] leading to a pondered value of 0.8 for a 50/50 mixture).

This ratio is also in line with the value that can be calculated according to the richness hypothesis proposed by Jain *et al.*[36] Indeed, the optimal ratios for the pure poles have been calculated to be CA/U = 10/18[32,38] and CA/Pu = 20/18,[37] and, considering a 50/50 mixture, the expected optimal ratio would be:

$$\frac{CA}{U+Pu} = 0.5 \times \frac{20}{18} + 0.5 \times \frac{10}{18} = \frac{15}{18} = 0.83$$

Therefore, the experimentally determined optimal CA/(U + Pu) ratios correspond to the expected values derived from the linear relationships determined for pure poles, as well as the theoretical values issued from Jain's theory.

In order to ensure the complete reduction of uranium during the combustion without an additional thermal treatment, a synthesis of $U_{0.5}Pu_{0.5}O_{2\pm x}$ was performed under a reducing atmosphere (ArH_2, 4%) instead of air. A CA/(U + Pu) ratio of 0.89 was chosen to optimize the combustion, according to the first part of this work. Under these conditions, the combustion does not require an external source of O_2 as an oxidant.[36] The diffraction pattern of the powder after the synthesis under a reducing atmosphere shows a solid solution as obtained in air (Fig. 2) with no evidence of a secondary uranium-rich phase. The formation of a solid solution indicates that the ignition and combustion occurred during the experiment, even in the absence of oxygen, which confirms the stoichiometric conditions.[36] The lattice parameter (a = 5.4157 ± 0.0001 Å) is closer to the theoretical one for $U_{0.5}Pu_{0.5}O_2$ (a = 5.4335 Å) than the powder synthesized under an air atmosphere (Table 1). This result highlights a better reduction of uranium(+VI) than when the syntheses were performed in air.

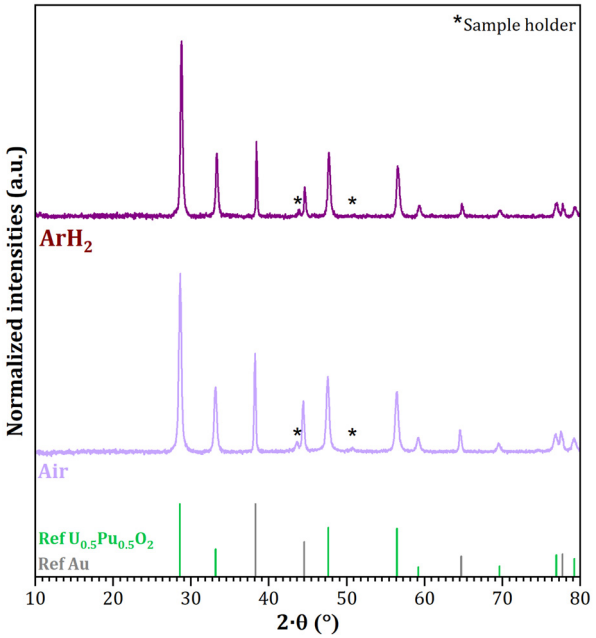

Fig. 2 X-ray diffraction patterns of the powder obtained under air and under a reducing atmosphere (ArH_2-4%) Pu/(U + Pu) = 50%.

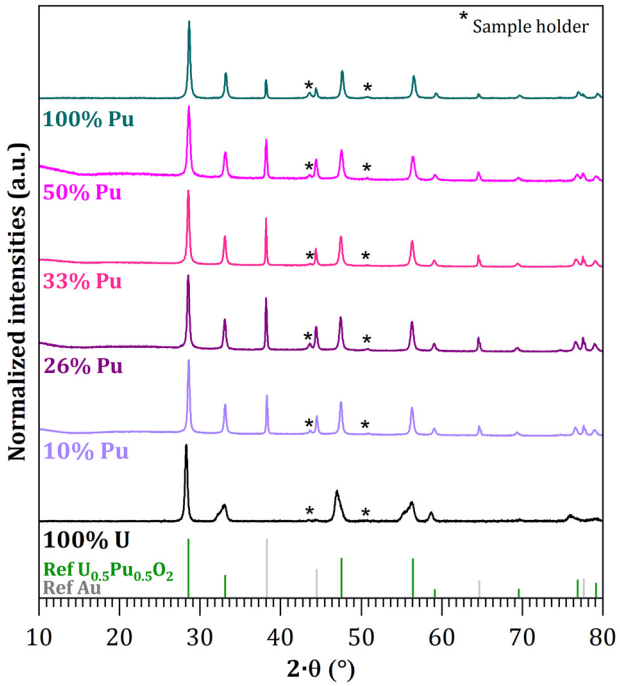

Fig. 3 X-ray diffraction patterns of $U_{1-y}Pu_yO_{2\pm x}$ powders obtained by citric acid assisted SCS.

However, this reduction is still incomplete, as the lattice parameters remain far from the reference value, and O/M = 2.00 was not reached. Therefore, it appears that the direct use of SCS under a reducing atmosphere does not allow a perfectly stoichiometric $(U,Pu)O_2$ oxide to be produced. Depending on the intended use of the powder, a further reducing treatment may be necessary to improve the characteristics of the oxides.

Effect of Pu/(U + Pu) composition

Mixed oxide syntheses were carried out with a variable Pu/(U + Pu) ratio ranging from 10 to 50 mol% in order to characterize the homogeneity of the powder obtained under optimal mixing conditions of citric acid and actinides. The obtained oxides all crystallized in a solid solution $U_{1-y}Pu_yO_{2\pm x}$ structure, as shown in the X-ray diffraction patterns presented in Fig. 3. The diffraction patterns do not exhibit any extra peaks that could indicate phase separation due to over-oxidation. In the case of the uranium oxide (100% uranium sample), the Bragg peaks corresponding to the (111) and (200) reflections are asymmetrical and present a shoulder respectively at 32.5° and 47°, which indicate a tetragonal distortion of the cubic lattice due to over-stoichiometry.[55,56] This deformation led to the tetragonal structure of U_3O_{7-x}, which was indeed identified for the uranium sample.[56]

However, the lattice parameters of the as-prepared mixed oxides are lower than those predicted, indicating an over-stoichiometric oxygen content (Fig. 4). This appears to affect the uranium cations as the deviation from the value expected for the stoichiometric oxide increased with the uranium content.

The over-oxidation is evidenced by the HERFD-XANES spectra at the uranium M_4 edge for the 26 mol% Pu and

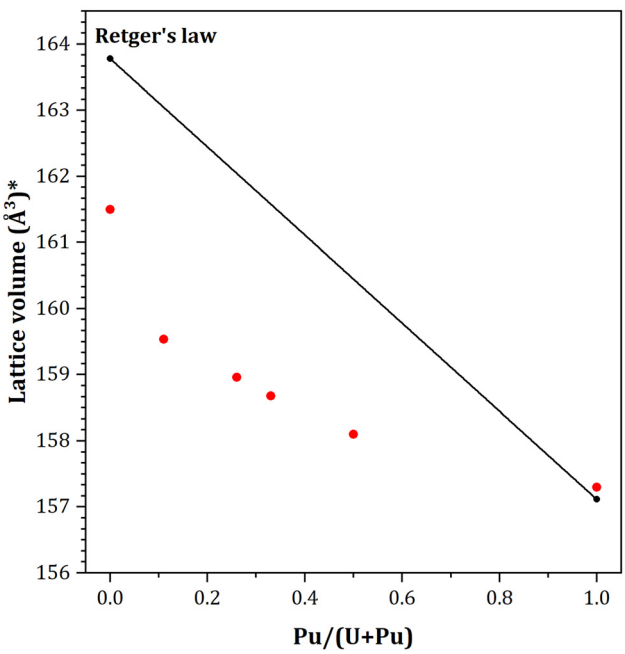

Fig. 4 Retger's law plot with lattice volume of the $U_{1-y}Pu_yO_{2\pm x}$ powders obtained by citric acid assisted SCS. *The unit cell volume of uranium oxide obtained by SCS is taken from a previous study,[38] and the values are presented in volume units to account for the over-oxidation of uranium oxide, which has resulted in a tetragonal distortion of the fluorite unit cell.[38,55]

Table 3 HERFD-XANES spectra recorded at uranium and plutonium M_4 edges for the $U_{0.74}Pu_{0.26}O_{2+x}$ powder, and deconvolution results

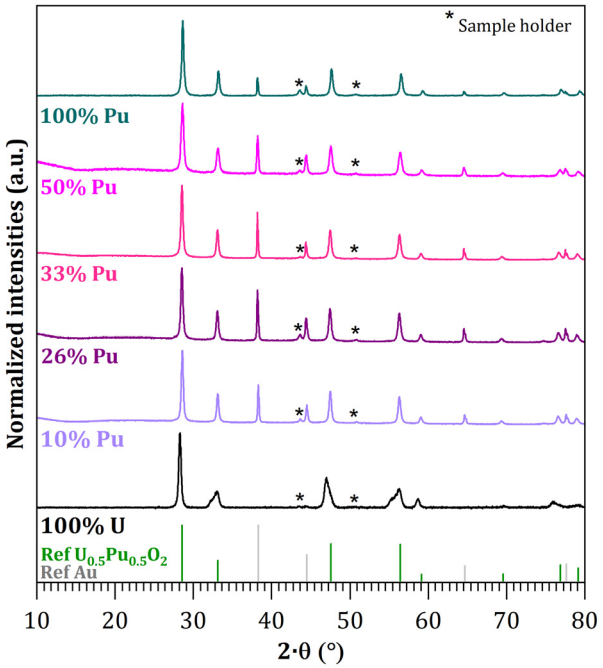

Oxidation state	Contribution in $U_{0.74}Pu_{0.26}O_{2+x}$ powder[a]
Uranium(IV)	1%
Uranium(V)	31%
Uranium(VI)	68%
Plutonium(III)	3%
Plutonium(IV)	79%
Plutonium(V)	18%
Plutonium(VI)	0%

[a] For the quantification of the different oxidation states, the error is estimated as 5%.

50 mol% Pu powders, which show contributions from uranium(+VI) and (+V) (Tables 2 and 3). The coexistence of uranium(+V) and uranium(+VI) is consistent with an oxygen excess in the structure, leading to a hyperstoichiometric oxide (O/M > 2), as expected from the PXRD results. Although the Pu M_4 edge spectra show the characteristic shape of plutonium (+IV), they also reveal the presence of a fraction of Pu(+V) in the $U_{0.74}Pu_{0.26}O_{2+x}$ and $U_{0.50}Pu_{0.50}O_{2+x}$. This contrasts with typical results reported for cubic $(U,Pu)O_{2\pm x}$ oxides synthesized by conventional methods, where plutonium is predominantly tetravalent,[57] or reduced into Pu(+III) after sintering.[58]

Moreover, the spectrum of the PuO_2 powder, also obtained by SCS with an optimal CA/Pu ratio (details of the synthesis are reported in previous work[37]), shows no evidence of plutonium(+V) in the PuO_2 end member. The presence of plutonium(+V) in the $(U,Pu)O_{2+x}$ mixed oxides does not appear to be correlated with the nanometric nature of the powders, since PuO_2 powder, which presents a close crystallite size, does not exhibit this oxidation state of Pu.

Therefore, overoxidation of plutonium is related to the overoxidation of uranium and the very specific conditions encountered in the SCS reaction. Indeed, this method is characterized by a near-instantaneous reaction under an air atmosphere,[30,54] which may limit the complete reduction of uranium cations initially present as U(+VI) in the uranyl nitrate precursor,[30] thus affecting the plutonium oxidation state. The SCS method, due to its exothermic and rapid character, may trap these intermediate oxidation states within the fluorite lattice, especially given the very small crystallite size (10–30 nm), limiting oxygen diffusion and cation rearrangement.

The carbon residual content of the oxides was determined using micro-gas chromatography analysis, and all were below 0.5% mass, which is consistent with oxides of actinides obtained by the SCS process without further thermal treatment[33,37] (Fig. 5).

SEM images do not appear to show significant differences in structure with changes in the plutonium content (Fig. 6). The powders form aggregates with a diameter of several hundred micrometers. A cross-sectional view of the material reveals a porous, foam-like structure (Fig. 6), similar to the sample containing 100 mol% Pu presented in a previous work.[37] However, the latter exhibited surface macroporosity

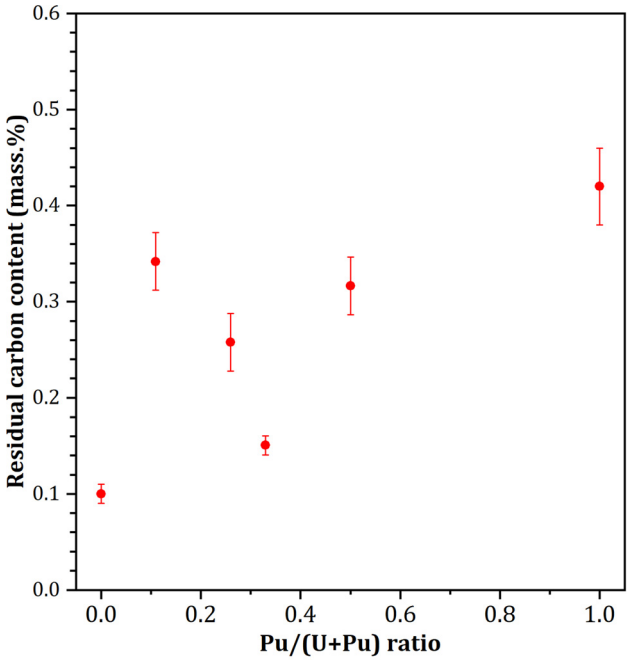

Fig. 5 Residual carbon content of the $U_{1-y}Pu_yO_{2\pm x}$ powders obtained by citric acid assisted SCS (determination by μ-GC).

in,[37] a phenomenon that is only observed in the sample with the highest plutonium content in this work (Fig. 6D).

The powders were calcined at 1100 °C under a reducing atmosphere (Ar-96%/H_2-4%) in order to verify the Pu/(U + Pu) content. The diffraction patterns indicate a recrystallization of the products (Fig. 7), which remain a solid phase solution. The lattice parameters after calcination evolve linearly between the two theoretical pure end members, UO_2 and PuO_2.[50–52] The additional calcination step under ArH_2 allows the uranium to be reduced, as indicated by the lattice parameter of the oxides after the thermal treatment (Fig. 7).

Pellet shaping and sintering of $U_{0.90}Pu_{0.10}O_{2+x}$

The $U_{0.90}Pu_{0.10}O_{2+x}$ powder was chosen because it is representative of the MOX used in PWR Generation III reactors. The fuel/metal ratio was selected to optimize the powder's characteristics toward pellet shaping and sintering. Analysis of the powder by laser granulometry before pelletizing shows a broad volume distribution of particle sizes (Fig. 8). The average volume particle size is 77 μm, which is consistent with the observations made by SEM (Fig. 6). The broad distribution of particle sizes is consistent with the manufacturing method. This can be explained by the absence of mechanical treatment of the powder (grinding), with the powder being de-agglomerated by hand in a mortar. The granulometric distribution allows for the identification of particles with a very high granulometry, corresponding to agglomerates.

The dilatometric curve of the pellet sintering indicates a low-temperature sintering (with a maximum shrinkage temperature at 800 °C). Most of the shrinkage thus occurs before 1000 °C, which is extremely low compared to the sintering behavior of powders prepared using powder metallurgy,[59] even when sintered in very oxidative atmospheres.[60] This can be correlated with the nanometer-scale dimensions of the powders prepared by the SCS process as well as with their high specific surface area, which is higher than the powders of enriched uranium oxide used for the fabrication of UO_2 fuel (6.6 $m^2\ g^{-1}$, compared to typically 2–3 $m^2\ g^{-1}$ for powder metallurgy[61]). A second shrinkage step can be observed starting around

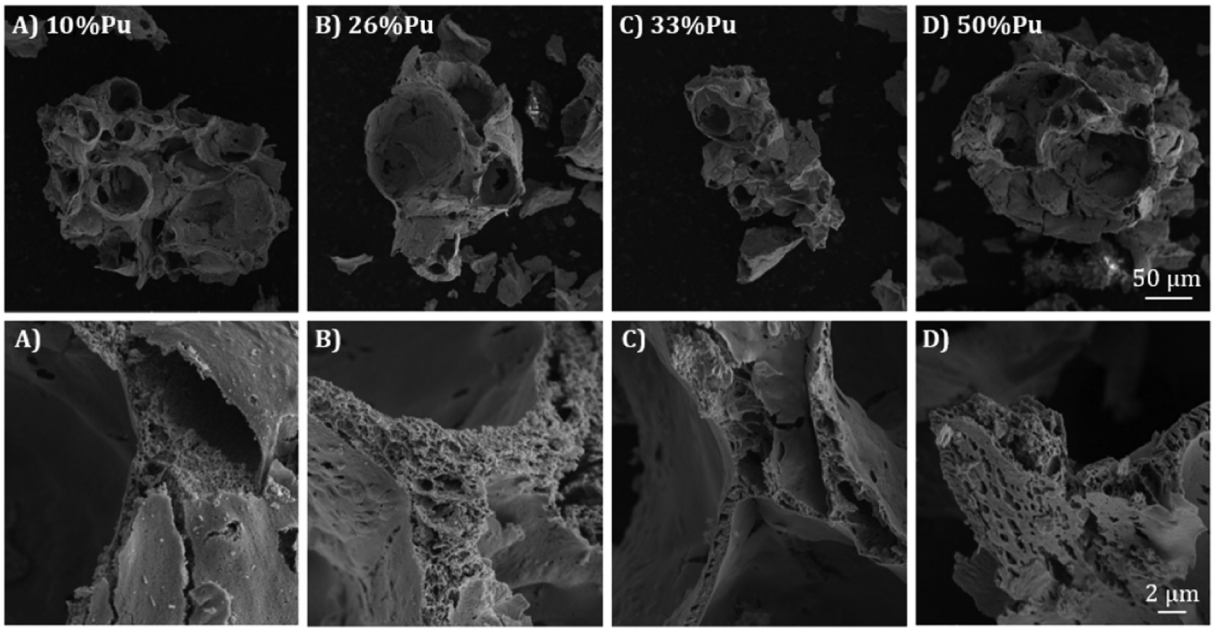

Fig. 6 SEM micrographs of $(U,Pu)O_{2\pm x}$ powders with Pu/(U + Pu) = (A) 10%, (B) 26%, (C) 33%, and (D) 50%.

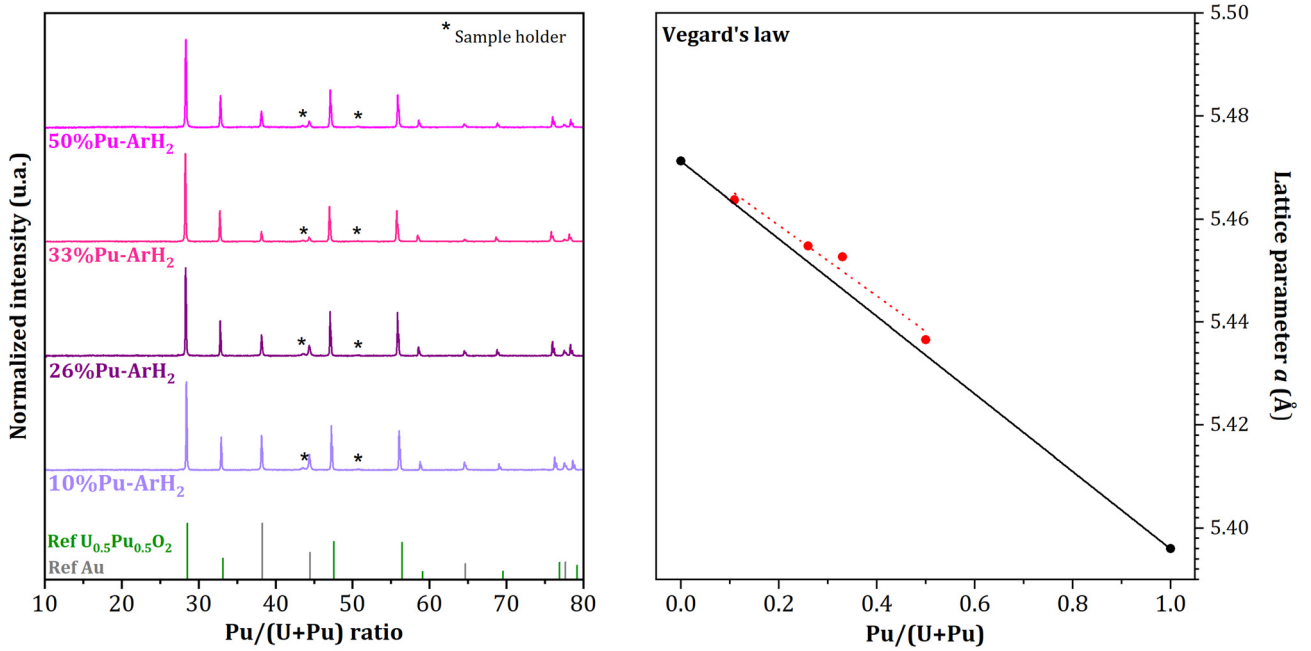

Fig. 7 X-ray diffraction patterns and lattice parameters of powders after calcination.

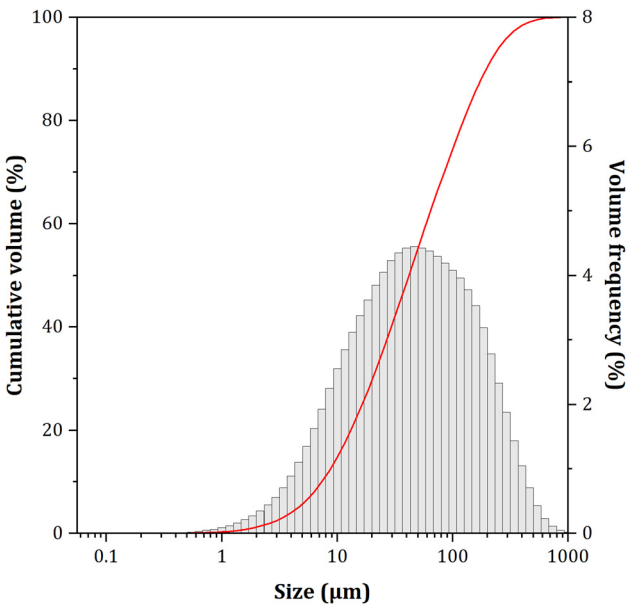

Fig. 8 Particle size distribution of the powder used for pellet fabrication.

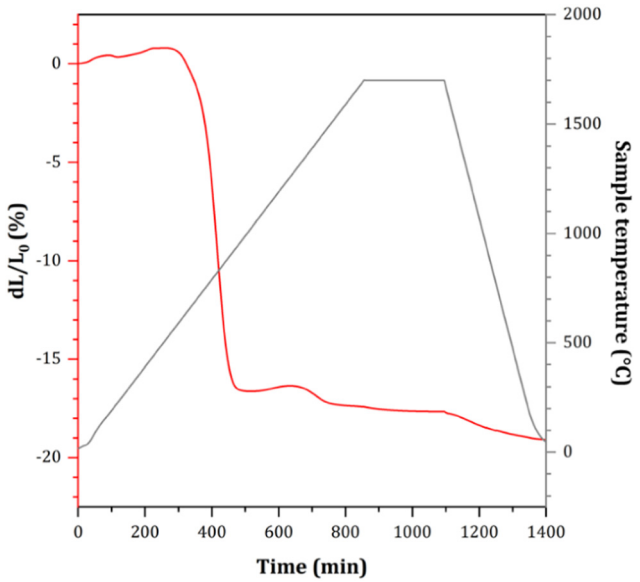

Fig. 9 Dilatometric analysis of the $U_{0.90}Pu_{0.10}O_{2+x}$ pellet in Ar 95.7%/H_2 4.3%.

1250 °C, which corresponds to the sintering temperature generally observed for MOX fuel.[10] Fig. 9 indicates an overall shrinkage of 19.1%, which is consistent with the geometrical measurement performed on the pellet with a 18.1% variation in height and 18.3% variation in diameter.

The density of the pellet was determined by the geometric method (86.7%TD) and the hydrostatic method (91.7%TD). Based on hydrostatic measurements, the open porosity was determined to be 3.3%, and the closed porosity was 5.0%, meaning a total porosity of 8.3%.

The optical micrographs of the longitudinal cut of the pellet show significant open and closed porosity. Imaging analysis reveals a total porosity of 15%, corresponding to a density of 85%. Two modes appear in the distribution: a first one centered on a few micrometers, which corresponds to the expected round-shaped microporosity observed in Fig. 10B, and a second one corresponding to macropores with an ECD larger

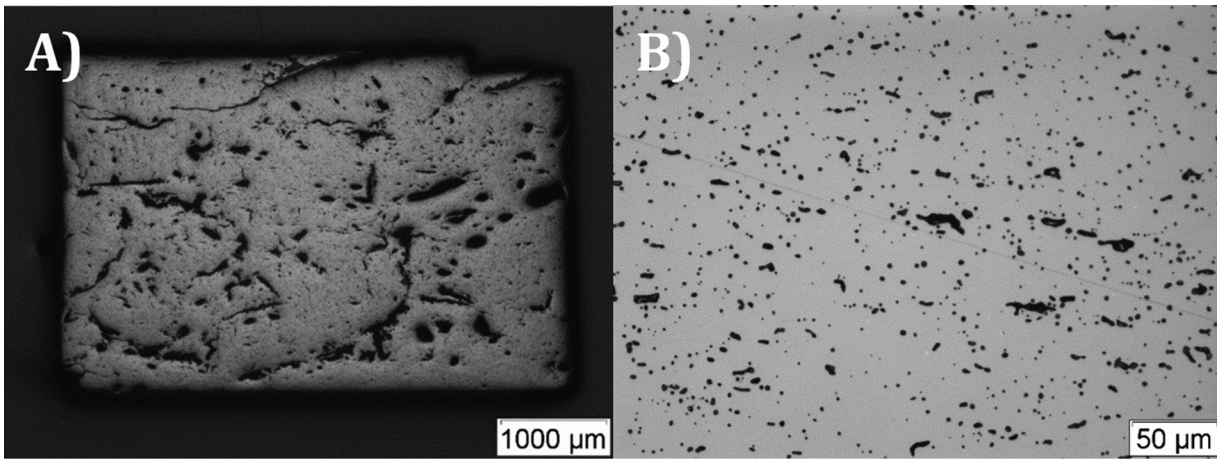

Fig. 10 Optical view of the polished cross-section of the $U_{0.90}Pu_{0.10}O_{2+x}$ pellet after sintering (longitudinal cut), (A) whole cross section showing the macropores, (B) detail showing the microstructure obtained between the macropores (the diagonal grey line is a scratch resulting from the sample preparation).

than 100 µm (Fig. 11). Considering the large size of the macropores, the open porosity might, however, be underestimated by the hydrostatic method, and the actual density might be closer to that measured by the geometric method.

The important and large porosity could be explained by the evacuation of organic residues from the powder (measured at 3000 ppm for the initial powder). Moreover, the oxidation state of uranium in the initial powder can influence the behavior during sintering and so the porosity, as the initial powder contains an important fraction of uranium(+VI). The residual organic content and the presence of uranium(+VI) induced a 5% weight-loss during sintering. Besides, the broad distribution size of the particles can lead to difficulties during pellet pressing. An additional grinding step or sieving could improve the pellet shaping and the behavior during sintering to reach higher pellet densities.

Element mapping analysis indicates a very homogeneous cationic distribution (Fig. 12) in perfect agreement with the analyses carried out on the precursor powder, which reveal a solid solution $(U,Pu)O_{2+x}$ in X-ray diffraction (Fig. 3). Fig. 13A presents the plutonium distribution extracted from the three 1 mm^2 maps (dots), compared to what would be obtained for a perfectly homogeneous sample (line). Almost no differences are observed between the sample and the theoretical homo-

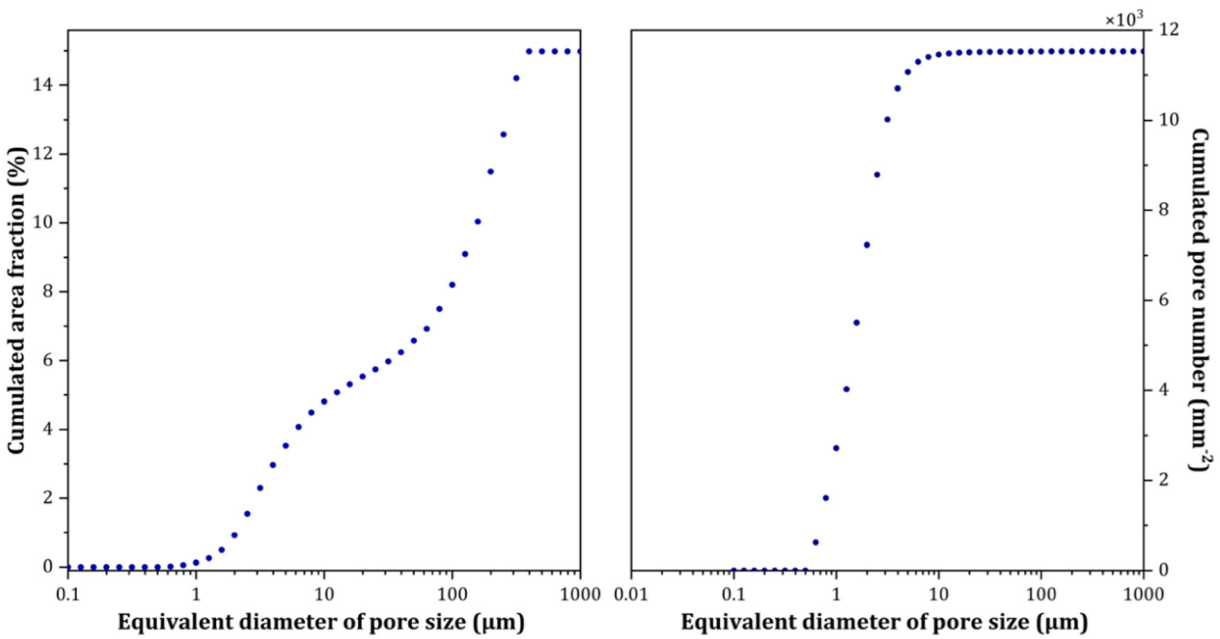

Fig. 11 Distribution of pore sizes in the $U_{0.90}Pu_{0.10}O_{2+x}$ pellet after sintering, determined using ImageJ software.

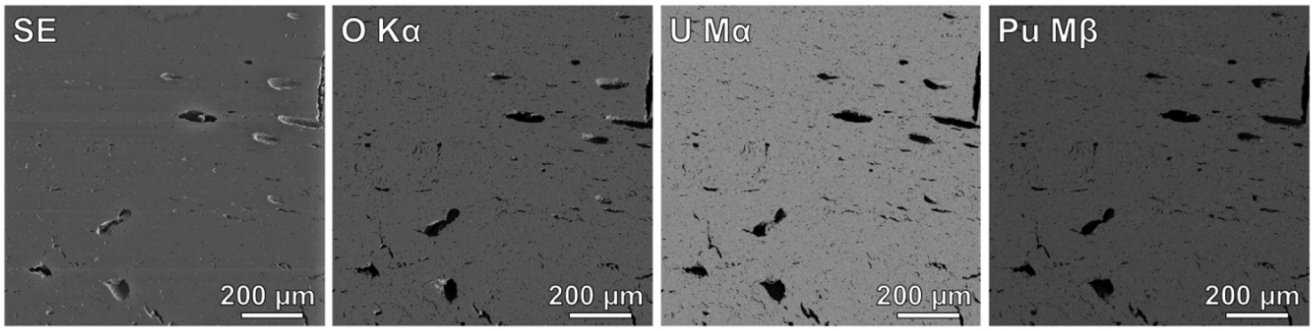

Fig. 12 SE (secondary electron), oxygen, uranium and plutonium mappings obtained by EPMA on the 512 × 512 µm^2 area polished cross-section of the sintered $U_{0.90}Pu_{0.10}O_{2+x}$ pellet.

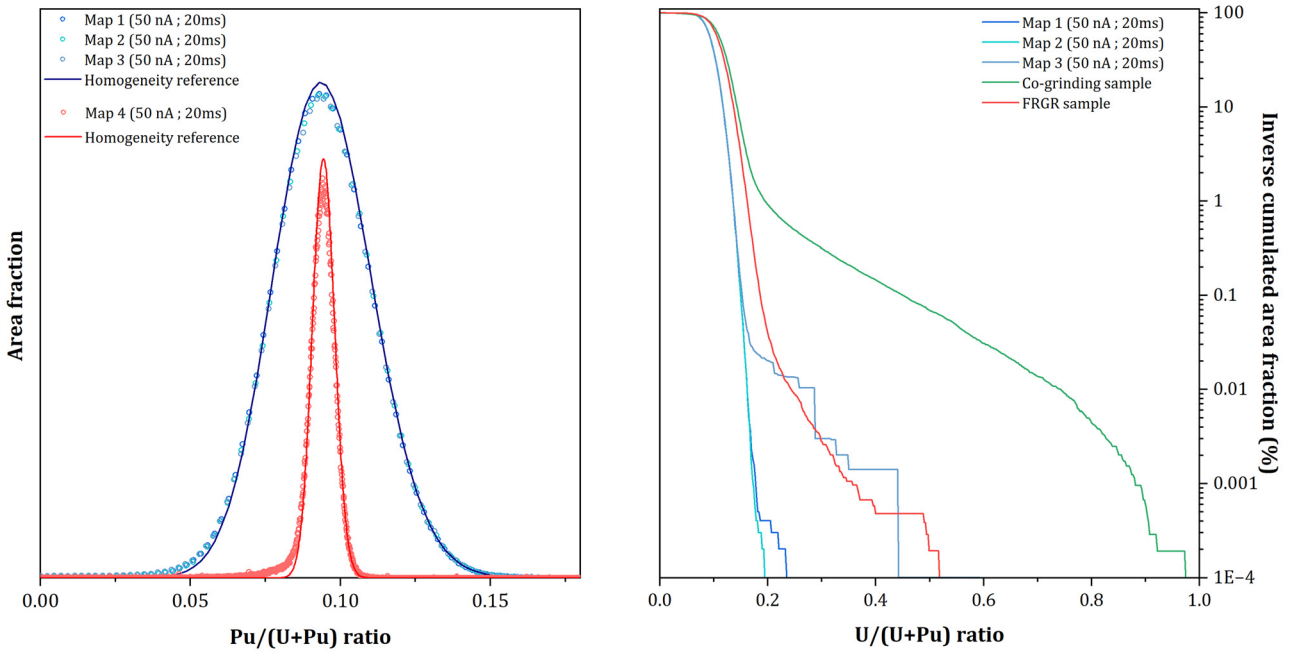

Fig. 13 (A) Pu content distribution extracted from the EPMA mappings compared to the expected distribution for a perfect homogeneity (broadening of the peak due to the measurement conditions). (B) inverse cumulated area fraction as a function of the Pu content extracted from the same three maps and compared to that obtained on two pellets fabricated from conventional UO_2 and PuO_2 powders.[59]

geneous reference. Even when the counting rate is significantly increased (by increasing the probe current and counting time; red curves in Fig. 13A), the only observable deviation from the perfect homogeneity is a small shoulder in the lower plutonium contents. Fig. 13B compares the inverse cumulative area fraction as a function of the plutonium contents for the three 1 mm^2 maps to that obtained in $(U_{0.90}Pu_{0.10})O_2$ pellets fabricated from powders prepared from UO_2 and PuO_2 (respectively through co-grinding and freeze granulation routes). This comparison highlights the absence of Pu-rich spots in the pellet obtained from the SCS method. Less than 0.01% of the mappings have Pu/(U + Pu) ratios greater than 20 wt%, whereas it is more than 1% for the sample obtained by co-grinding.

The average signal of 1851 Raman spectra is shown in Fig. 14 (left). This spectrum is typical of a fluorite-type structure, as observed in UO_2, PuO_2 and $(U,Pu)O_2$.[48,62–66] No other band corresponding to a hypothetical secondary phase can be seen. The main bands observed correspond to the T_{2g} mode at 449.6 ± 0.5 cm^{-1}, the T_{1u} (LO) at 575.8 ± 0.5 cm^{-1} and 2LO at 1152.1 ± 0.5 cm^{-1}. The presence of the T_{1u} (LO) band, which is not activated for a perfect fluorine structure, is attributed to a slight local distortion due to the difference in ionic radii between uranium(+IV) and plutonium(+IV).[48] As shown by Medyk *et al.*,[67] the position of the T_{2g} line in a $(U,Pu)O_{2-x}$ structure is directly linked to the plutonium content and the O/M ratio. Using the Medyk *et al.*[67] relation for a stoichiometric compound (O/M = 2.00), a 449.6 ± 0.5 cm^{-1} position corresponds to 9.4% ± 0.3% Pu/(U + Pu). This is the same value determined by EPMA, as shown in Fig. 13. The dispersion of the T_{2g} band position over the 1851 spectrum col-

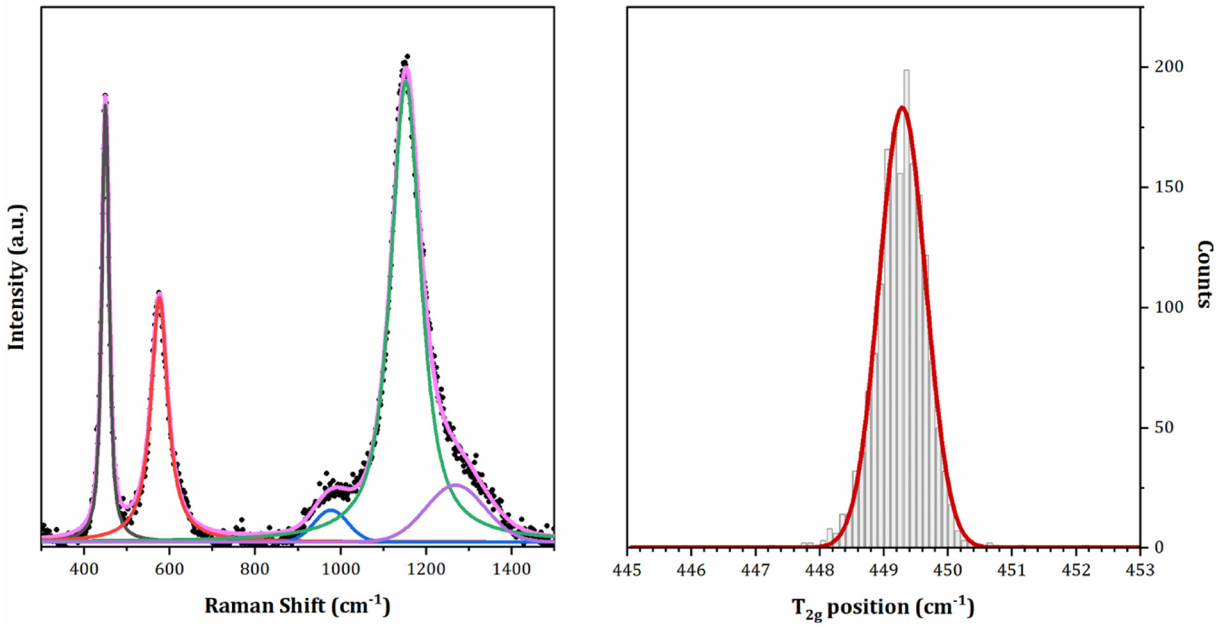

Fig. 14 Left: Average Raman spectra collected on the $U_{0.90}Pu_{0.10}O_2$ pellet. Right: Position dispersion of the T_{2g} band in the 1851 Raman spectra.

lected is plotted in Fig. 14 (right). This curve corresponds almost perfectly to a Gaussian distribution as shown by the fit (Fig. 14, right), with a maximum at 449.3 cm^{-1} and a full width at half maximum of 0.7 cm^{-1}. The slight difference between the average spectrum and distribution is within the uncertainty. Nevertheless, considering the 9.4% plutonium content measured by EPMA, a T_{2g} band at 449.3 cm^{-1} corresponds to an O/M ratio of 1.9985. The O/M ratio of the sample can be considered equal to 2.00, given the experimental uncertainty of the Raman analysis, and this oxygen stoichiometry is homogeneous over the whole pellet.

Conclusion

The synthesis of mixed oxides $(U,Pu)O_{2+x}$ by the SCS method using citric acid as a fuel was carried out. This choice was based on the promising results obtained on UO_2 [32,38] and PuO_2.[37] A parametric study on the amount of fuel was conducted to determine the optimal CA/An ratio required to trigger the ignition. The characterization of the powders produced by SCS under optimal conditions showed the formation of a homogeneous solid solution for all tested plutonium concentrations (Pu/(U + Pu) = 10, 26, 33 and 50 mol%). The obtained oxides presented a high over-stoichiometry due to the over-oxidation of uranium, which was characterized by PXRD and confirmed by HERFD-XANES. The presence of plutonium(+V) revealed by HERFD-XANES results is interesting because it had not been observed in PuO_2 that was also synthesized by SCS and had similar characteristics, such as crystallite size. This could be attributed to the specific conditions encountered during the SCS reaction and the presence of highly oxidized uranium in the lattice, which could stabilize Pu(+V). To better understand this phenomenon and precisely characterize the local structure around Pu and U atoms, several complementary approaches can be used. Especially, EXAFS spectroscopy, which is sensitive to distortions induced by Pu(+V) and U(+VI), could help to accurately determine interatomic distances and local coordination.

A sintering test of a $U_{0.90}Pu_{0.10}O_2$ pellet was carried out under conditions representative of the MOX of PWR reactors of Generation III. A density of 88%TD (geometric measurement) with homogeneous cationic distribution was achieved. Although the $(U,Pu)O_{2+x}$ powder prepared by the SCS method exhibits high over-stoichiometry, the final O/M ratio obtained in the sintered pellet is 2.00. This result demonstrates the feasibility of manufacturing stoichiometric pellets from powder obtained by the SCS method under conditions similar to those currently used in MOX manufacture. The very low sintering temperature is indicative of the nanocrystalline nature of the powders, a characteristic of the SCS. These results constitute a solid basis for optimizing the synthesis of mixed oxide powders of actinides and the subsequent step of pellet fabrication to obtain $(U,Pu)O_2$ pellets with more than 95%TD.

This work demonstrates the feasibility of the synthesis of actinide mixed oxides by the SCS method using citric acid as fuel. However, adjustments are necessary to control the stoichiometry of the as-prepared oxides produced, for example, by controlling the synthesis atmosphere or considering subsequent thermal treatment. In addition, a better understanding of the combustion phenomenon could allow the optimization of the amount of fuel in the mixture and thus minimize the amount of organic residues in the final powders. Although

the feasibility of sintering has been demonstrated on a single example, future work is needed to optimize fuel fabrication to produce dense pellets of MOX fuel.

Conflicts of interest

There are no conflicts to declare.

Data availability

The data supporting this article have been included as part of the supplementary information (SI). Supplementary information is available.[68–70] See DOI: https://doi.org/10.1039/d5dt02138c.

Acknowledgements

The authors would like to thank L. Barnouin for supporting the SEM analyses, M. Verger for supporting the pellet characterization, C. Aloin for supporting the Raman analysis and M. Alibert and C. Aloin for the sample preparation for the HERFD-XANES experiment. The authors would like to thank the technical support staff at the ESRF for their assistance during the experiment on the ROBL beamline. This work has been funded by CEA.

References

1 J. M. Cleveland, *The Chemistry of Plutonium*, American Nuclear Society, Second printing, 555 N. Kensington Ave., La Grange Park, IL 60625 USA, 1979.
2 D. Greneche, Cycle du combustible nucléaire : aval du cycle et questions génériques, Techniques de l'ingénieur, Génie Nucléaire, 2016, BN3564, DOI: 10.51257/a-v1-bn3564.
3 M. Salvatores, Physics and safety of transmutation systems, Chapter 1: P&T and the role of ADS, OECD Nuclear Energy Agency, NEA, 6090, 2006.
4 J.-D. Barbat and R. Liberge, Nuclear Fuel Cycle: Which strategy to support a sustainable growth for nuclear energy?, *Energy Procedia*, 2013, **39**, 69–80.
5 C. Poinssot, C. Rostaing, S. Grandjean and B. Boullis, Recycling the Actinides, The Cornerstone of Any Sustainable Nuclear Fuel Cycles, *Procedia Chem.*, 2012, **7**, 349–357, DOI: 10.1016/j.proche.2012.10.055.
6 G. Oudinet, *et al.*, Characterization of plutonium distribution in MIMAS MOX by image analysis, *J. Nucl. Mater.*, 2008, **375**, 86–94, DOI: 10.1016/j.jnucmat.2007.10.013.
7 P. Roy and C. Ganguly, Plutonium metallurgy in India, *Bull. Mater. Sci.*, 1984, **6**, 923–958.
8 D. Haas, A. Vandergheynst, J. Van Vliet, R. Lorenzelli and J.-L. Nigon, Mixed-oxide fuel fabrication technology and experience and CFCa plants and further developments for the Melox plant, *Nucl. Technol.*, 1994, **106**, 60–82.
9 R. Lerch and R. E. Norman, Nuclear Fuel Conversion and Fabrication Chemistry, *Radiochim. Acta*, 1984, **36**, 75–88.
10 M. Kato, Uranium Oxide and MOX manufacture, in *Comprehensive Nuclear Materials*, Elsevier, 2nd edn, 2020, pp. 2.
11 F. Abraham, B. Arab-Chapelet, M. Rivenet, C. Tamain and S. Grandjean, Actinide oxalates, solid state structures and applications, *Coord. Chem. Rev.*, 2014, **266–267**, 28–68, DOI: 10.1016/j.ccr.2013.08.036.
12 K. Asakura, K. Takeuchi, T. Makino and Y. Kato, Feasibility Study on a Simplified MOX Pellet Fabrication Process, the Short Process, for Fast Breeder Reactor Fuel, *Nucl. Technol.*, 2009, **167**(3), 3, DOI: 10.13182/NT09-A9075.
13 R. Eastman and S. Tod, *Microstructure of unirradiated SBR MOX fuel*, British Nuclear Fuels, Seascale, United Kingdom, IAEA-SM-358/9, 1999.
14 D. N. Bykhovskii, M. A. Kuz'mina and G. S. Novikov, Processes for preparing mixed oxides, as applied to conditions of spent nuclear fuel reprocessing without complete separation of U and Pu, *Radiochemistry*, 2010, **52**(2), 2, DOI: 10.1134/S1066362210020025.
15 M. Koizumi, K. Ohtsuka, H. Isagawa, H. Akiyama and A. Todokoro, Development of a Process for the Co-Conversion of Pu-U Nitrate Mixed Solutions to Mixed-Oxide Powder Using a Microwave Heating Method, *Nucl. Technol.*, 1983, **61**(1), 1, DOI: 10.13182/NT83-A33143.
16 J. Hobbs and P. Parkes, Production of MOX pellets from plutonia and mixed oxide powders prepared by direct thermal denitration, presented at the International conference Scientific research on the back-end of the fuel cycle for the 21. century, Atalante 2000, Avignon, France, 2000.
17 M. Leblanc, G. Leturcq, E. Welcomme, X. Deschanels and T. Delahaye, Actinide mixed oxide conversion by advanced thermal denitration route, *J. Nucl. Mater.*, 2019, **519**, 157–165.
18 B. Arab-Chapelet, S. Grandjean, G. Nowogrocki and F. Abraham, Synthesis of new mixed actinides oxalates as precursors of actinides oxide solid solutions, *J. Alloys Compd.*, 2007, **444–445**, 387–390, DOI: 10.1016/j.jallcom.2007.01.033.
19 C. Tamain, B. Arab Chapelet, M. Rivenet, F. Abraham, R. Caraballo and S. Grandjean, Crystal Growth and First Crystallographic Characterization of Mixed Uranium(IV)–Plutonium(III) Oxalates, *Inorg. Chem.*, 2013, **52**(9), 9, DOI: 10.1021/ic302587t.
20 G. Loubert, *et al.*, Quantitative Precipitation of Uranyl or Plutonyl Nitrate with N-(1-Adamantyl)acetamide in Nitric Acid Aqueous Solution, *Inorg. Chem.*, 2020, **59**, 11459–11468.
21 N. Hibert, B. Arab Chapelet, M. Rivenet, L. Venault, C. Tamain and O. Tougait, Coprecipitation of actinide peroxide salts in the U–Th and U–Pu systems and their thermal decomposition, *Dalton Trans.*, 2022, **51**, 12928–12942, DOI: 10.1039/d2dt02376h.
22 S. Benarib, N. Dacheux, X. F. Le Goff, J. Lautru, L. D. Mascio and N. Clavier, Hydrothermal conversion of

mixed uranium(IV)–cerium(III) oxalates into $U_{1-x}Ce_xO_{2+\delta}{\cdot}nH_2O$ solid solutions, *Dalton Trans.*, 2023, **52**(31), 10951–10968, DOI: 10.1039/D3DT01510F.

23 P. A. Haas, R. D. Arthur, and W. B. Stines, *Development of thermal denitration to prepare uranium oxide and mixed oxides for nuclear fuel fabrication*, Oak ridge national laboratory, ORNL-5735, 1981.

24 A. G. Merzhanov, The chemistry of self-propagating high-temperature synthesis, *J. Mater. Chem.*, 2004, **14**(12), 12, DOI: 10.1039/b401358c.

25 J. J. Kingsley and K. C. Patil, A novel combustion process for the synthesis of fine particle α-alumina and related oxide materials, *Mater. Lett.*, 1988, **6**(11), 11, DOI: 10.1016/0167-577X(88)90045-6.

26 K. C. Patil, S. T. Aruna and T. Mimani, Combustion synthesis: an update, *Curr. Opin. Solid State Mater. Sci.*, 2002, **6**(6), 6, DOI: 10.1016/S1359-0286(02)00123-7.

27 A. Varma, A. S. Mukasyan, A. S. Rogachev and K. V. Manukyan, Solution Combustion Synthesis of Nanoscale Materials, *Chem. Rev.*, 2016, **116**(23), 23, DOI: 10.1021/acs.chemrev.6b00279.

28 F. Deganello, Nanomaterials for environmental and energy applications prepared by solution combustion based-methodologies: Role of the fuel, *Mater. Today: Proc.*, 2017, **4**(4), 4, DOI: 10.1016/j.matpr.2017.06.006.

29 K. V. Manukyan, *et al.*, Solution Combustion Synthesis of Nano-Crystalline Metallic Materials: Mechanistic Studies, *J. Phys. Chem. C*, 2013, **117**(46), 46, DOI: 10.1021/jp408260m.

30 J. M. Roach, *et al.*, Hyperstoichiometric Uranium Dioxides: Rapid Synthesis and Irradiation-Induced Structural Changes, *Inorg. Chem.*, 2021, **60**(24), 24, DOI: 10.1021/acs.inorgchem.1c02736.

31 A. E. Danks, S. R. Hall and Z. Schnepp, The evolution of 'sol–gel' chemistry as a technique for materials synthesis, *Mater. Horiz.*, 2016, **3**(2), 2, DOI: 10.1039/C5MH00260E.

32 J. Monnier, *Conversion des nitrates d'actinides en oxydes par combustion en solution, Université de Montpellier*, CEA Marcoule, 2019.

33 D. Maji, *et al.*, Nanocrystalline $(U_{0.5}Ce_{0.5})O_{2\pm x}$ solid solutions through citrate gel-combustion, *J. Nucl. Mater.*, 2018, **502**, 370–379, DOI: 10.1016/j.jnucmat.2017.10.007.

34 R. D. Purohit, B. P. Sharma, K. T. Pillai and A. K. Tyagi, Ultrafine ceria powders via glycine-nitrate combustion, *Mater. Res. Bull.*, 2001, **36**(15), 15, DOI: 10.1016/S0025-5408(01)00762-0.

35 A. S. Mukasyan, P. Epstein and P. Dinka, Solution combustion synthesis of nanomaterials, *Proc. Combust. Inst.*, 2007, **31**(2), 2, DOI: 10.1016/j.proci.2006.07.052.

36 S. R. Jain, K. C. Adiga and V. R. Pai Verneker, A new approach to thermochemical calculations of condensed fuel-oxidizer mixtures, *Combust. Flame*, 1981, **40**, 71–79, DOI: 10.1016/0010-2180(81)90111-5.

37 A. Hautecouverture, P. Estevenon, C. Rey and X. Deschanels, Synthesis of plutonium dioxide by citric acide-assisted Solution Combustion Synthesis, *J. Nucl. Mater.*, 2023, **586**, 154694–154699.

38 A. Hautecouverture, *Synthèse de solution solide d'oxydes mixtes d'actinides par Combustion en Solution*, Université de Montpellier, 2023.

39 A. Jain, K. Ananthasivan, S. Anthonysamy and P. R. Vasudeva Rao, Synthesis and sintering of $(U_{0.72}Ce_{0.28})O_2$ solid solution, *J. Nucl. Mater.*, 2005, **345**(2–3), 2–3, DOI: 10.1016/j.jnucmat.2005.06.007.

40 R. Venkata Krishnan, *et al.*, Synthesis, characterization and thermal expansion measurements on uranium–cerium mixed oxides, *J. Nucl. Mater.*, 2011, **414**(3), 3, DOI: 10.1016/j.jnucmat.2011.05.010.

41 G. Peter Soldani, *Approche structurale et phénoménologique de la conversion directe ou modifiée de nitrate d'actinide(s) en oxyde*, Université de Lille, 2013.

42 L. M. Rösken, *et al.*, Time-dependent growth of crystalline Au0-nanoparticles in cyanobacteria as self-reproducing bioreactors: 1. Anabaena sp., *J. Nanopart. Res.*, 2014, **16**(4), 4, DOI: 10.1007/s11051-014-2370-x.

43 J. Rodriguez-Carvajal, Recent developments of the program FULLPROF, Comm. Powder Diffr. IUCr Newsl., 2001, vol. 26, pp. 12–19.

44 A. C. Scheinost, *et al.*, ROBL-II at ESRF: a synchrotron toolbox for actinide research., *J. Synchrotron Radiat.*, 2021, **28**(Pt 1), 333–349, DOI: 10.1107/S1600577520014265.

45 K. O. Kvashnina and A. C. Scheinost, A Johann-type X-ray emission spectrometer at the Rossendorf beamline, *J. Synchrotron Radiat.*, 2016, **23**(3), 836–841, DOI: 10.1107/S1600577516004483.

46 J. Schindelin, *et al.*, Fiji: an open-source platform for biological-image analysis, *Nat. Methods*, 2012, **9**(7), 676–682, DOI: 10.1038/nmeth.2019.

47 D. Drouin, A. R. Couture, D. Joly, X. Tastet, V. Aimez and R. Gauvin, CASINO V2.42—A Fast and Easy-to-use Modeling Tool for Scanning Electron Microscopy and Microanalysis Users, *Scanning*, 2007, **29**(3), 92–101, DOI: 10.1002/sca.20000.

48 O. Kahraman, F. Lebreton, P. Martin and M. Mermoux, Observable consequences of self-irradiation damage in a MIMAS-type MOX nuclear fuel as analyzed by X-ray diffraction, electron microprobe analysis, and Raman imaging. A possible methodological approach, *J. Appl. Phys.*, 2022, **132**, 115106.

49 D. Sanjay Kumar, K. Ananthasivan, R. Venkata Krishnan, S. Amirthapandian and A. Dasgupta, Bulk synthesis of nanocrystalline urania powders by citrate gel-combustion method, *J. Nucl. Mater.*, 2016, **468**, 178–193, DOI: 10.1016/j.jnucmat.2015.10.054.

50 G. Fournet, Étude de la loi de Vegard, *J. Phys. Radium.*, 1953, **14**(6), 6, DOI: 10.1051/jphysrad:01953001406037400.

51 G. Leinders, T. Cardinaels, K. Binnemans and M. Verwerft, Accurate lattice parameter measurements of stoichiometric uranium dioxide, *J. Nucl. Mater.*, 2015, **459**, 135–142, DOI: 10.1016/j.jnucmat.2015.01.029.

52 M. Beauvy, Nonideality of the solid solution in $(U, Pu)O_{2\pm x}$ nuclear fuels, *J. Nucl. Mater.*, 1992, **188**, 232–238.

53 P. Fouquet-Métivier, *et al.*, Insight into the Cationic Charge Distribution in $U_{1-y-z}Pu_yAm_zO_{2\pm x}$ Mixed Oxides, *Inorg. Chem.*, 2024, **63**(43), 20482–20491, DOI: 10.1021/acs.inorgchem.4c03084.
54 F. Deganello and A. K. Tyagi, Solution combustion synthesis, energy and environment: Best parameters for better materials, *Prog. Cryst. Growth Charact. Mater.*, 2018, **64**(2), 2, DOI: 10.1016/j.pcrysgrow.2018.03.001.
55 G. Rousseau, *et al.*, A detailed study of UO_2 to U_3O_8 oxidation phases and the associated rate-limiting steps, *J. Nucl. Mater.*, 2006, **355**(1–3), 1–3, DOI: 10.1016/j.jnucmat.2006.03.015.
56 G. Leinders, R. Delville, J. Pakarinen, T. Cardinaels, K. Binnemans and M. Verwerft, Assessment of the U_3O_7 Crystal Structure by X-ray and Electron Diffraction, *Inorg. Chem.*, 2016, **55**(19), 19, DOI: 10.1021/acs.inorgchem.6b01941.
57 P. Martin, *et al.*, XAS characterisation of xenon bubbles in uranium dioxide, *Nucl. Instrum. Methods Phys. Res., Sect. B*, 2008, **266**(12–13), 12–13, DOI: 10.1016/j.nimb.2008.03.180.
58 P. Fouquet-Métivier, *et al.*, Investigation of the solid/liquid phase transitions in the U–Pu–O system, *CALPHAD*, 2023, **80**, 102523, DOI: 10.1016/j.calphad.2022.102523.
59 G. Bernard-Granger, *et al.*, Comparative sintering behaviour of MOX powders synthesized through the freeze granulation or dry-cogrinding routes, *J. Eur. Ceram. Soc.*, 2024, **44**(12), 7224–7235, DOI: 10.1016/j.jeurceramsoc.2024.05.016.
60 G. C. C. Miranda, *et al.*, MOX fuel sintering under oxidizing conditions: A comprehensive study of the solarisation phenomenon, *J. Eur. Ceram. Soc.*, 2023, **43**(14), 6373–6385, DOI: 10.1016/j.jeurceramsoc.2023.06.072.
61 J. Siméon, *Frittage et développement de la microstructure du combustible nucléaire MOX RNR*, Université Grenoble Alpes, 2022.
62 J. M. Elorrieta, L. J. Bonales, N. Rodríguez-Villagra, V. G. Baonza and J. Cobos, A detailed Raman and X-ray study of UO_{2+x} oxides and related structure transitions, *Phys. Chem. Chem. Phys.*, 2016, **18**(40), 40, DOI: 10.1039/C6CP03800J.
63 M. J. Sarsfield, R. J. Taylor, C. Puxley and H. M. Steele, Raman spectroscopy of plutonium dioxide and related materials, *J. Nucl. Mater.*, 2012, **427**(1–3), 1–3, DOI: 10.1016/j.jnucmat.2012.04.034.
64 E. Villa-Alleman, N. J. Bridges, T. C. Shehee and A. L. Houk, Raman microscopy of PuO_2 particulate aggregates, *J. Nucl. Mater.*, 2019, **515**, 140–149.
65 O. A. Maslova, *et al.*, Raman imaging and principal component analysis-based data processing on uranium oxide ceramics, *Mater. Charact.*, 2017, **129**, 260–269.
66 M.-M. Desagulier, J. Martinez, P. M. Martin, F. Lebreton, C. Guéneau and N. Clavier, Multi-scale structural investigation of uranium-plutonium mixed oxides $(U_{1-y}Pu_y)O_{2-x}$ with high plutonium content, *J. Nucl. Mater.*, 2023, **585**, 154645.
67 L. Medyk, *et al.*, Determination of the plutonium content and O/M ratio of $(U,Pu)O_2$-xusing Raman spectroscopy, *J. Nucl. Mater.*, 2020, **541**, 152439.
68 C. Madic, D. E. Hobart and G. M. Begun, Raman spectrometric studies of Actinide(V) and -(VI) complexes in aqueous sodium carbonate solution and of solid sodium Actinide(V) carbonate compounds, *Inorg. Chem.*, 1983, **22**, 1494–1503.
69 I. Pidchenko, J. März, M. O. J. Y. Hunault, S. Bauters, S. M. Butorin and K. O. Kvashnina, Synthesis, Structural, and Electronic Properties of $K_4PuVIO_2(CO_3)_3$(cr): An Environmentally Relevant Plutonium Carbonate Complex, *Inorg. Chem.*, 2020, **59**, 11889–11893.
70 G. Leinders, R. Bes, J. Pakarinen, K. Kvashnina and M. Verwerft, Evolution of the Uranium Chemical State in Mixed-Valence Oxides, *Inorg. Chem.*, 2017, **56**, 12.